



ATLAS CONF Note

ATLAS-CONF-2017-017



Search for long-lived charginos based on a disappearing-track signature in pp collisions at $\sqrt{s} = 13$ TeV with the ATLAS detector

The ATLAS Collaboration

31st March 2017

This paper presents a search for direct electroweak gaugino or gluino pair production with the chargino nearly mass-degenerate with a stable neutralino. It is based on the integrated luminosity of 36.1 fb^{-1} of pp collisions collected at $\sqrt{s} = 13$ TeV by the ATLAS experiment at the LHC. The final state of interest is a disappearing track accompanied by at least one jet with high transverse momentum from initial state radiation or by four jets from the gluino decay chain. The use of short track segments reconstructed from the innermost tracking layers significantly improves the sensitivity to short chargino lifetimes. The results are found to be consistent with Standard Model predictions. Exclusion limits are set at 95% confidence level on the mass of charginos and gluinos for different chargino lifetimes. For a pure wino with a lifetime of about 0.2 ns, chargino masses up to 430 GeV are excluded. For the strong production channel, gluino masses up to 1.6 TeV are excluded assuming a chargino mass of 430 GeV and lifetime of 0.2 ns.



1 Introduction

Supersymmetry (SUSY) [1–6] is a space-time symmetry that relates fermions and bosons. It predicts new particles that differ from their Standard Model (SM) partners by a half unit of spin. If R-parity is conserved [7], SUSY particles are produced in pairs and decay such that their final products consist only of SM particles and the stable lightest supersymmetric particle (LSP). In many supersymmetric models, the supersymmetric partners of the SM boson W fields, the wino fermions, are the lightest gaugino states. This implies that the lightest chargino is nearly mass-degenerate with the LSP, and its lifetime can be long enough to have measurable effects. For example, Anomaly Mediated Supersymmetry Breaking (AMSB) scenarios [8, 9] naturally predict a pure wino LSP. The mass splitting between the charged and neutral wino in such models is suppressed at tree-level by the approximate custodial symmetry; it has been calculated at the two-loop level to be around 160 MeV [10], corresponding to a chargino lifetime of about 0.2 ns [11]. This prediction for the value of the lifetime is actually a general feature of models with a wino LSP: within the generated models of the ATLAS phenomenological Minimal Supersymmetric Standard Model (pMSSM) scan [12] that have a wino-like LSP, about 70% have a charged wino lifetime in between 0.15 ns and 0.25 ns. Most of the models in the other 30% have a larger mass splitting (and therefore the charged wino has a shorter lifetime) due to a non-decoupled higgsino mass. The search presented here is sensitive to a wide range of lifetimes, from 10 ps to 10 ns, and reaches maximum sensitivity around 0.2 ns.

The decay products of SUSY particles that are highly mass degenerate with the lightest neutralino leave little visible energy in the detector. Thus the corresponding searches represent a significant challenge for the LHC experiments. If a charged SUSY particle produced in a high energy collider acquires a relatively long lifetime, it will leave multiple hits¹ in the traversed tracking layers before decaying, and can then be reconstructed as a track segment in the innermost part of the detector [13–15]. A long-lived chargino usually decays to a pion and the LSP, a neutralino. The pion emitted in the $\tilde{\chi}_1^\pm \rightarrow \tilde{\chi}_1^0$ transition typically has very low momentum and simulation has shown that it is not reconstructed in the detector, and the neutralino is assumed to pass through the detector without interacting. A track arising from a long-lived chargino can therefore *disappear*, that is, leave hits only in the innermost layers and no hits in the portions of the detector at higher radii. Figure 1 shows an example of a simulated electroweak production event in which a long-lived chargino decays into a neutralino and a low-momentum pion in the ATLAS detector.

Previous searches for a disappearing-track signature were performed by the ATLAS [16] and CMS [17] collaborations using the full dataset of the LHC pp run at a centre of mass energy of $\sqrt{s} = 8$ TeV. These searches excluded chargino masses below 270 GeV and 260 GeV, respectively, for a proper lifetime of 0.2 ns.

In the previous ATLAS analysis, the search was sensitive to charginos decaying at radii larger than about 30 cm. A crucial improvement in the analysis described here is the use of much shorter tracks. The use of these tracks is possible thanks to the new innermost tracking layer installed during the LHC long shutdown between Run-1 and Run-2. The use of shorter tracks significantly extends the sensitivity to small chargino lifetimes. The analysis is performed by searching for an excess of observed events with a high transverse momentum (p_T), short track in event samples featuring large missing transverse momentum, whose magnitude is referred to as E_T^{miss} , and high p_T jets. The background spectrum shape and yields are estimated using a data-driven method.

¹ A hit is a spacetime point which represents interactions between a particle and material in an active region of a particle detector.

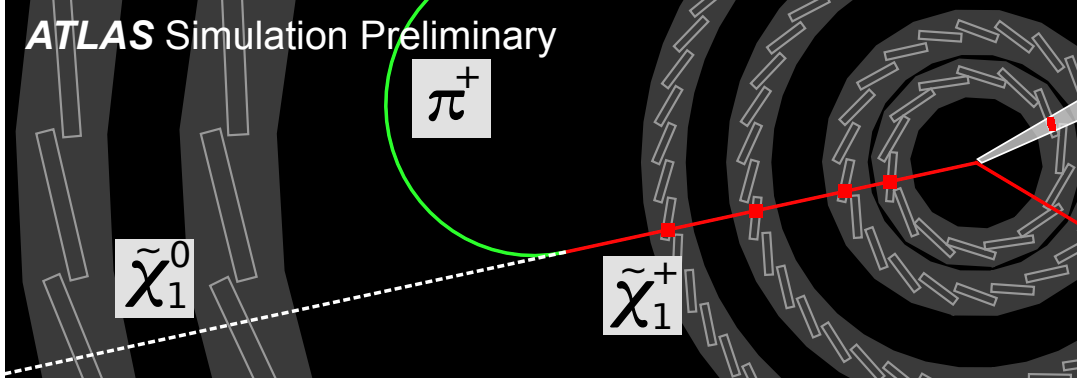


Figure 1: Simulated $pp \rightarrow \tilde{\chi}_1^+ \tilde{\chi}_1^- + \text{jet}$ event, with long-lived charginos. The $\tilde{\chi}_1^+$ decays into a low-momentum pion and a $\tilde{\chi}_1^0$ after leaving hits in the four pixel layers.

Two signal processes are studied in this paper. One search targets direct electroweak gaugino pair production where the final state contains a disappearing track, a jet from initial state radiation, and $E_{\text{T}}^{\text{miss}}$. The second search targets gluino pair production with a final state composed of a disappearing track, four jets, and $E_{\text{T}}^{\text{miss}}$.

This paper is organised as follows. A brief overview of the ATLAS detector is given in Section 2. In Section 3, the signal processes (electroweak pair-production of charginos and strong pair-production of gluinos) are described. The data samples used in this analysis and the simulation model of the signal processes are described in Section 4. The reconstruction algorithms and event selection are presented in Section 5. The analysis method is discussed in Section 6. The systematic uncertainties are described in Section 7. The results are presented in Section 8. Section 9 is devoted to conclusions.

2 The ATLAS detector

ATLAS [18] is a multipurpose detector with a forward-backward symmetric cylindrical geometry, covering nearly the entire solid angle around a collision point of the LHC.² The inner tracking detector (ID) consists of pixel and micro-strip silicon detectors covering the pseudorapidity region of $|\eta| < 2.5$, surrounded by a transition radiation tracker (TRT), which improves the momentum measurement and enhances electron identification capabilities. The pixel detector spans the radius range from 3 to 12 cm, the strip semiconductor tracker (SCT) from 30 to 52 cm, and the TRT from 56 to 108 cm. The pixel detector has four barrel layers and three disks in the forward and backward directions. The barrel layers surround the beam pipe at radii of 33.3, 50.5, 88.5, and 122.5 mm, covering $|\eta| < 1.9$. These layers are equipped with pixel read-out elements with a pitch of 50 μm in the transverse direction. The pitch sizes in the longitudinal direction are 250 μm for the first layer and 400 μm for the other layers. The innermost layer, the insertable B-layer [19, 20], was added during the first long shutdown, and improves the reconstruction of short tracks

² ATLAS uses a right-handed coordinate system with its origin at the nominal interaction point in the centre of the detector. The positive x -axis is defined by the direction from the interaction point to the centre of the LHC ring, with the positive y -axis pointing upwards, while the beam direction defines the z -axis. Cylindrical coordinates (r, ϕ) are used in the transverse plane, ϕ being the azimuthal angle around the z -axis. The pseudorapidity η is defined in terms of the polar angle θ by $\eta = -\ln \tan(\theta/2)$ and the rapidity is defined as $y = (1/2) \ln[(E + p_z)/(E - p_z)]$ where E is the energy and p_z the longitudinal momentum of the object of interest.

by adding an additional measurement point close to the interaction region. The pixel end-caps cover up to pseudo-rapidities of ± 2.5 with three disks on each side of the barrel. The ID is surrounded by a thin superconducting solenoid providing an axial 2 T magnetic field and by a fine-granularity lead/liquid-argon (LAr) electromagnetic calorimeter covering $|\eta| < 3.2$. The calorimeters in the forward region of $3.1 < |\eta| < 4.9$ are made of LAr active layers with either copper or tungsten as the absorber material. A steel/scintillator-tile calorimeter provides coverage for hadronic showers in the central pseudorapidity range of $|\eta| < 1.7$. LAr hadronic end-cap calorimeters, which use lead as absorber, cover the forward region of $1.5 < |\eta| < 3.2$. The muon spectrometer with an air-core toroid magnet system surrounds the calorimeters. Three stations of high-precision tracking chambers provide coverage in the range of $|\eta| < 2.7$, while dedicated chambers allow triggering in the region of $|\eta| < 2.4$. The ATLAS trigger system [21] consists of a hardware-based level-1 trigger followed by a software-based high level trigger.

3 Description of the signal processes

If the gluino mass is too large to yield a sizeable production cross-section, electroweak-gaugino direct pair production could be the only gaugino production mode within reach at LHC energies. If the gluino mass is relatively light, however, gluino pair production becomes the dominant process, and charginos can be produced in cascade decays of the gluino. For large mass separations between the gluino and the chargino, the relatively large p_T transferred to the chargino typically leads to tighter kinematic selection efficiencies and larger chargino decay radii relative to charginos from gaugino pair production. Two complementary searches are described here: one targets direct electroweak-gaugino pair production and the other targets gluino pair production in which at least one long-lived chargino is produced in the subsequent decay of the gluinos.

Electroweak production This analysis is based on the production processes $pp \rightarrow \tilde{\chi}_1^\pm \tilde{\chi}_1^0 j$ and $pp \rightarrow \tilde{\chi}_1^+ \tilde{\chi}_1^- j$, where j denotes an energetic jet from initial state radiation (ISR). The presence of the ISR jet is required to ensure significant E_T^{miss} and hence high trigger efficiency. An example diagram for the $pp \rightarrow \tilde{\chi}_1^\pm \tilde{\chi}_1^0 j$ process is presented in Figure 2 (a). The resulting signal topology is characterised by a high- p_T jet, large E_T^{miss} , and at least one high- p_T disappearing track.

Strong production This search targets gluino pair production with a long-lived chargino in the decay chains $pp \rightarrow \tilde{g}\tilde{g} \rightarrow qq\tilde{\chi}_1^\pm \tilde{\chi}_1^0$ and $pp \rightarrow \tilde{g}\tilde{g} \rightarrow qq\tilde{\chi}_1^\pm \tilde{\chi}_1^\pm$. These are typical decay modes in AMSB models. An example diagram is shown in Figure 2 (b). The signal topology is characterised by four high- p_T jets, large E_T^{miss} , and at least one high- p_T disappearing track.

4 Data and simulated event samples

The data used in this analysis were recorded by the ATLAS detector in 2015 and 2016. The centre of mass energy was 13 TeV and the bunch spacing was 25 ns.

Events are selected by E_T^{miss} triggers [22] with trigger thresholds varying from 70 GeV to 110 GeV depending on the data-taking period. Auxiliary data samples used to estimate the background events and to measure tracking performance were selected using triggers requiring at least one isolated electron

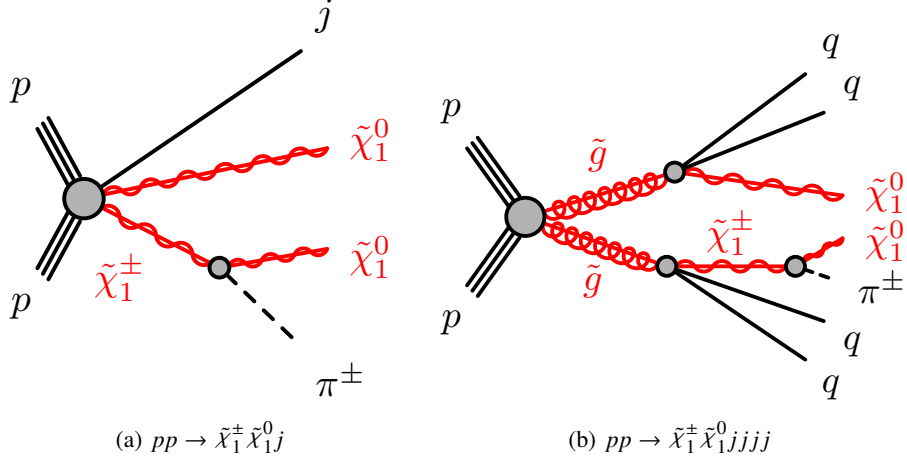


Figure 2: Example diagrams of the benchmark signal processes used in this analysis. In the case of direct chargino/neutralino production (a), the signal signature consists of a long-lived chargino and initial state radiation. In the case of the strong channel (b), each gluino decays to two quarks and a chargino or neutralino. A long-lived chargino and multiple quarks, which are observed as jets, are the signatures of this signal.

($p_T > 24\text{--}26$ GeV) or muon ($p_T > 24\text{--}26$ GeV). After applying basic data quality requirements, the data sample corresponds to an integrated luminosity of 36.1 fb^{-1} . The uncertainty in the combined 2015+2016 integrated luminosity is 3.2%. It is derived, following a methodology similar to that detailed in Ref. [23], from a preliminary calibration of the luminosity scale using x - y beam-separation scans performed in August 2015 and May 2016.

The simulated signal samples are generated assuming the minimal AMSB model [8, 9] with the ratio of the Higgs vacuum expectation values at the electroweak scale set to $\tan \beta = 5$, the sign of the higgsino mass term set to be positive, and the universal scalar mass set to $m_0 = 5$ TeV. The proper lifetime and the mass of the chargino are scanned in the range from 10 ps to 10 ns and from 100 GeV to 700 GeV respectively. For the strong production, samples are generated for gluino masses varying from 700 GeV to 2200 GeV with LSP mass from 200 GeV to $m_{\tilde{g}} - 100$ GeV. The SUSY mass spectrum, the branching ratios and decay widths are calculated using ISASUSY ver.7.80 [24]. The signal samples are generated with up to two extra partons in the matrix element using MG5_aMC@NLO 2.3.3 [25] at leading order (LO) interfaced to PYTHIA 8.186 [26] for parton shower, hadronisation and SUSY particle decay. The NNPDF2.3LO [27] parton distribution function (PDF) set is used. Renormalisation and factorisation scales are determined by the default dynamic scale choice of MG5_aMC@NLO. The CKKW-L merging scheme [28] is applied to combine tree-level matrix elements containing multiple partons with parton showers. A scale parameter for merging is set to a quarter of the mass of the wino for the wino-pair production or a quarter of the gluino mass for the strong production channel. The A14 [29] set of tuned parameters with simultaneously optimised multiparton interaction (MPI) and parton shower (ISR, FSR) parameters is used for underlying event together with the NNPDF2.3LO PDF set. Charginos are forced to decay into a pion and a neutralino.

The cross sections of the electroweak production are calculated at the next-to-leading order (NLO) in the strong coupling constant using PROSPINO2 [30]. The cross sections of the strong production are calculated in the same way as in the electroweak channel, adding the resummation of soft gluon emission at next-to-leading-logarithmic accuracy (NLO+NLL) [31]. In both channels, an envelope of cross-section

predictions is defined using the 68% CL ranges of the CTEQ6.6 PDF [32], including the α_s uncertainty, and MSTW2008 [33] PDF sets, together with variations of the factorisation and renormalisation scales by factors of two or one half. The nominal cross-section value is taken to be the midpoint of the envelope and the uncertainty assigned is half of the full width of the envelope, following the PDF4LHC recommendations [34]. For the strong production mode, the branching ratio of the gluino decay is assumed to be 1/3 for $\tilde{g} \rightarrow qq\tilde{\chi}^0$, $\tilde{g} \rightarrow qq\tilde{\chi}^-$ and $\tilde{g} \rightarrow qq\tilde{\chi}^+$. Only light flavour quarks (d, u, s, c) are considered. Direct electroweak-gaugino production is not considered in the strong channel. The cross section for the electroweak production, including at least one chargino varies, from 47 pb to 13 fb as the wino mass increases from 100 GeV to 700 GeV with the uncertainty on the cross section ranging from 8.6% to 7.3%. The cross section of the gluino production varies from 3.5 pb to 0.36 pb as the gluino mass increases from 700 GeV to 2200 GeV with the uncertainty increasing from 14% to 36%.

The response of the detector to particles is modelled with the full ATLAS detector simulation [35] based on GEANT4 [36]. All simulated events are overlaid with additional pp interactions in the same and neighbouring bunch crossing (pile-up) simulated with the soft QCD processes of PYTHIA 8.186 using the A2 set of tuned parameters [37] and the MSTW2008LO [33] PDF set. The simulated events are reconstructed in the same way as the data, and are reweighted so that the distribution of the average number of collisions per bunch crossing matches the one observed in the data.

The E_T^{miss} trigger efficiency, which is applied to the simulated signal samples, is measured as a function of the offline E_T^{miss} using a data control sample consisting of events selected by the muon triggers and additional offline selections designed to extract nearly pure $W \rightarrow \mu\nu$ events. For $E_T^{\text{miss}} > 200$ GeV, the trigger efficiency is almost 100%. The trigger efficiency for the direct electroweak production signal is about 20%, depending on the assumed SUSY particle masses. In the strong production search, the trigger efficiency is over 90% when the mass difference between the gluino and the LSP is above 300 GeV, and it decreases to about 55% for a mass difference of 100 GeV.

5 Reconstruction and event selection

5.1 Event reconstruction

Primary vertices are reconstructed from two or more tracks, with $p_T > 400$ MeV. When two or more vertices are reconstructed, the one with the largest sum of p_T^2 of the associated tracks is used. Events are required to have at least one reconstructed primary vertex.

Jets are reconstructed from noise-suppressed energy clusters [38] of calorimeter cells using an anti- k_t algorithm [39, 40] with a distance parameter of 0.4. An area-based correction is applied to account for energy from additional pp collisions based on an estimate of the pile-up activity in a given event [41]. Further corrections derived from the average jet response in simulation and data are used to calibrate the jet energies to the scale of their constituent particles [42]. Jets are required to have $p_T > 20$ GeV and $|\eta| < 2.8$. Additional selection criteria are applied to the tracks associated to jets [43] with $p_T < 60$ GeV and $|\eta| < 2.4$ to reduce the number of jets originating from pile-up interactions.

Muon candidates are reconstructed by combining a track reconstructed by the muon spectrometer (MS track) with one recorded by the ID. They are required to satisfy ‘Medium’ quality requirements described in Ref. [44] and to have $p_T > 10$ GeV and $|\eta| < 2.7$.

Electron candidates are reconstructed from energy clusters in the electromagnetic calorimeter [45] with a matching track in the ID. They are required to satisfy the ‘Loose’ likelihood-based identification criteria described in Ref. [46]. They are further required to have transverse energy $E_T > 10$ GeV and $|\eta| < 2.47$.

After the requirements described above, ambiguities between candidate jets and leptons are resolved as follows. First, any jet candidate which is not tagged as a b -jet [47, 48] and which is within a distance $\Delta R \equiv \sqrt{(\Delta\eta)^2 + (\Delta\phi)^2} = 0.2$ of an electron candidate is discarded. Second, if a jet candidate is b -tagged, the object is interpreted as a jet and the overlapping electron is ignored. Third, if an electron (muon) candidate and a jet are found within $0.2 \leq \Delta R < 0.4$ ($\Delta R < \min(0.4, 0.04 + 10 \text{ GeV}/p_T^\mu)$), the object is interpreted as a jet and the nearby electron (muon) candidate is discarded. Finally, if a muon and a jet are found within $\Delta R < 0.2$, the object is treated as a muon and the overlapping jet is ignored if fewer than three tracks with $p_T > 500$ MeV are associated to the jet. These four criteria are intended to identify jets consistent with final state radiation or hard bremsstrahlung. In addition, ambiguities between electrons and muons are resolved to avoid double counting: an electron is discarded if the electron candidate and a muon candidate share the same ID track.

The missing transverse momentum [49] is calculated based on the transverse momenta of selected jets, lepton candidates, and tracks compatible with the primary vertex that are not associated to such objects.

Track reconstruction is performed in two stages. First, tracks are reconstructed using a standard algorithm [50]. Standard tracks are required to have at least seven hits in the silicon detectors [51]. The track reconstruction is then rerun with looser criteria, requiring at least four pixel-detector hits. The second reconstruction uses only hits not associated with standard tracks as input, in order to reconstruct short tracks which are not reconstructed in the first step. Tracks reconstructed in the second step are hereafter referred to as tracklets. The tracklets are then extrapolated to the SCT and TRT detectors, and any compatible hits are associated to the tracklet candidate. Tracklets are required to have $p_T > 5$ GeV, $|\eta| < 2.2$, and their longitudinal impact parameter with respect to the primary vertex, $|z_0|$, must be smaller than 10 mm. Tracklets with no hits in the SCT are referred to as pixel tracklets. Figure 3 shows the chargino reconstruction efficiency as a function of its decay radius in the simulation. Requirements described later in this section are not applied to compute the efficiency except for the disappearing condition for pixel tracklets. By using pixel tracklets rather than standard tracks, the reconstruction efficiency is improved significantly for charginos decaying at radii shorter than 300 mm. For charginos with a lifetime of 0.2 ns, the reconstruction efficiency using pixel tracklets is 5–10%, which is a factor of ten greater than the efficiency obtained using standard tracks. The remaining inefficiency is largely due to charginos which decay before reaching the fourth layer of the pixel detector.

To reduce contributions from “fake” tracklets which do not originate from a single particle, the following requirements are applied to the tracklets:

- (1) **Isolation and p_T requirement:** The angular separation ΔR between the tracklet and any jets with $p_T > 50$ GeV or tracks reconstructed by the muon spectrometer must be greater than 0.4. A track or tracklet is defined as isolated when the sum of the p_T of all standard ID tracks with $p_T > 1$ GeV and $|z_0 \sin(\theta)| < 3.0$ mm in a cone of $\Delta R = 0.4$ around the track or tracklet, divided by the track or tracklet p_T , is small: $p_T^{\text{cone40}}/p_T < 0.04$. The candidate tracklet is required to be isolated. The candidate tracklet must have $p_T \geq 20$ GeV, and the p_T must be the highest among isolated tracks and tracklets in the event.
- (2) **Quality requirement:** The tracklet is required to have hits on all four pixel layers. The number of pixel holes, defined as missing hits on layers where at least one is expected given the detector

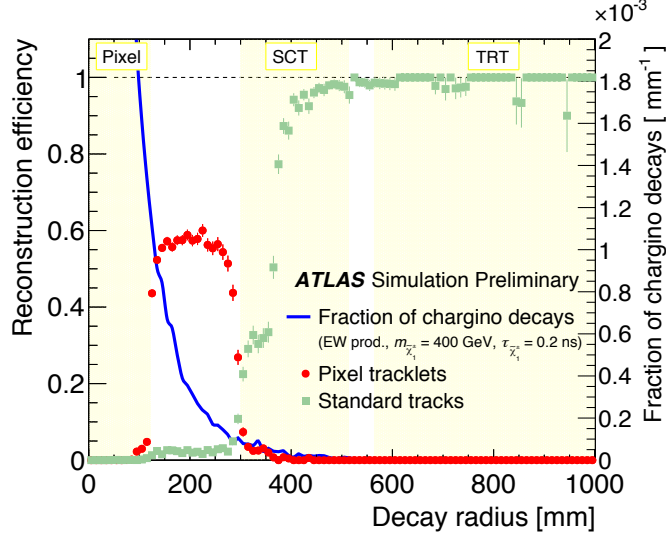


Figure 3: Chargino reconstruction efficiency as a function of decay radius. The distribution of the decay radius for charginos with a lifetime of 0.2 ns is shown in blue. The reconstruction efficiency of pixel tracklets before applying the fake-rejection criteria is shown in red, while that obtained with the standard tracking algorithm is shown in green. The yellow shaded regions correspond to the coverage of each detector.

geometry and conditions, must be zero. The number of low quality hits³ associated to the tracklet must be zero. Furthermore, tracklets must satisfy requirements on the significance of the transverse impact parameter, d_0 , with respect to the beam line, $|d_0|/\sigma(d_0) < 2$ (where $\sigma(d_0)$ is the uncertainty of the d_0 measurement), and $|z_0 \sin(\theta)| < 0.5$ mm. The χ^2 -probability of the fit is required to be larger than 10%.

(3) **Geometrical acceptance:** The tracklet must satisfy $0.1 < |\eta| < 1.9$.

(4) **Disappearing condition:** The number of SCT hits associated to the tracklet must be zero.

The isolation and quality requirements are mainly useful to reduce fake tracklets, which typically tend to have large impact parameters. The requirement on η excludes tracklets with $\eta \sim 0$, where the muon spectrometer has low efficiency. Including tracklets in this region would increase the background significantly, as the lepton rejection is less efficient. Tracklets with $|\eta| > 1.9$ are rejected because the probability of a particle scattered by detector material to be reconstructed as a tracklet increases with $|\eta|$. The disappearing condition is used to identify tracklets which disappear between the pixel and the SCT detectors. The selection efficiency for chargino tracks is about 90% and 65% to 70% for the requirements (1) and (2) respectively, assuming a chargino lifetime of 0.2 ns, and varies depending on the chargino mass. The inefficiency of the quality requirements is mostly due to temporarily inactive modules of the pixel detector. The number of background events is reduced by four orders of magnitude by applying requirements (1) and (2). The signal efficiency is 85% to 90% and 75% to 85% for requirements (3) and (4), respectively, for a chargino lifetime of 0.2 ns. After all the selection requirements, the signal efficiency is 4% for electroweak production of a 400 GeV chargino with a lifetime of 0.2 ns. In the strong production

³ A hit is categorised as low quality when the single hit position uncertainty is large, or the hit position is far from the reconstructed tracklet.

mode, the efficiency varies from 0.5% to 6% for a chargino with a lifetime of 0.2 ns, depending on the chargino mass.

5.2 Event selection

Events are selected by applying requirements on the event kinematics. The selection requirements for the signal regions for the two different production channels are described below.

Event preselection Common selection criteria are required in both searches. One pixel tracklet is required satisfying all the requirements described in Section 5.1. To ensure good quality data, all jets in the event are required to satisfy ‘LooseBad’ quality criteria [52] and events containing a muon with momentum uncertainty $\sigma(q/p)/|q/p| > 0.2$ are rejected, where q and p are the electric charge and the magnitude of the momentum of the muon. To suppress contributions from top-quark-pair ($t\bar{t}$) and W/Z +jets production processes, candidate events are required to have no electron and no muon candidates (lepton veto).

Electroweak chargino production: Events are required to have $E_T^{\text{miss}} > 140$ GeV and at least one jet with $p_T > 140$ GeV to discriminate the signal from SM processes. In order to further suppress the multijets background, the difference in azimuthal angle ($\Delta\phi$) between E_T^{miss} and each of the up to four highest- p_T jets with $p_T > 50$ GeV is required to be larger than 1.0. The efficiency of the electroweak event selection is about 40% for benchmark signal model events with a chargino mass of 400 GeV and a lifetime of 0.2 ns which satisfy the trigger requirements. Only about 1% of the triggered events in data satisfy the event selection, as the data are dominated by background events.

Strong production: Candidate events are required to have $E_T^{\text{miss}} > 150$ GeV, a jet with $p_T > 100$ GeV and at least two additional jets with $p_T > 50$ GeV to discriminate the signal from SM processes. In order to further suppress the multijets background, the $\Delta\phi$ between E_T^{miss} and each of the up to four highest- p_T jets with $p_T > 50$ GeV is required to be larger than 0.4. For signals with large mass differences between the gluino and the LSP, the selection efficiency is about 70%, while it decreases to about 30% when the mass difference is as small as 100 GeV. The fraction of triggered events in data passing the event selection is about 0.2%.

6 Estimate of signal and background

To test the data for the signal hypothesis, an unbinned likelihood fit is performed on the p_T distribution of the tracklets in a wide p_T range from 20 GeV to 12.5 TeV. The fit is performed simultaneously on events in a high- E_T^{miss} region, which is defined by the requirements described in Section 5, and in a low- E_T^{miss} region, for which the requirement on E_T^{miss} is replaced by $90 \text{ GeV} < E_T^{\text{miss}} < 140 \text{ GeV}$ ($100 \text{ GeV} < E_T^{\text{miss}} < 150 \text{ GeV}$) for the electroweak (strong) channel. Most of the signal events are expected to be in the high- E_T^{miss} region. The contamination of signal in the low- E_T^{miss} region is at the level of 3%, and this region is used to constrain the fake tracklet p_T spectrum.

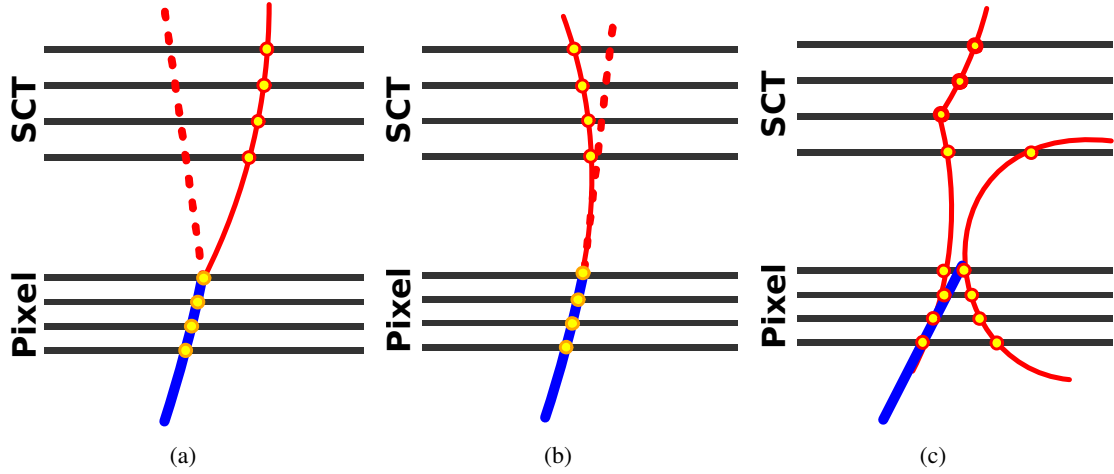


Figure 4: Sketch of the different background components to the search for pixel tracklets. Thin solid and dotted red lines show trajectories of charged and neutral particles respectively. Thick blue lines show reconstructed pixel tracklets. (a) A hadron undergoing a hard scattering can yield track segments in the pixel and SCT detector that are not recognised as belonging to the same track, thus faking a disappearing tracklet. (b) A lepton emitting hard photon radiation could be identified as a disappearing tracklet through a similar mechanism. (c) Finally, a disappearing tracklet can arise from a random combination of hits created by different nearby particles.

6.1 Signal and background templates

The main SM background processes for the two analysis channels are from $t\bar{t}$ and W +jets (with $W \rightarrow e\nu, \tau\nu$) production, where the electrons or the hadrons, usually pions, come from the τ leptons. Hadrons or leptons can be classified as a tracklet if they interact with the detector material and any hits in the tracking detectors after the pixel detector are not associated to the reconstructed track. This may happen because of severe multiple-scattering, hadronic interactions or, in the case of leptons, bremsstrahlung. Another category of background is fake tracklets, which originate from random combinations of hits from more than two particles. A schematic view of the three background categories are shown in Figure 4.

Templates for these background components are estimated from data. The p_T spectra of hadrons and leptons scattered by the ID material are estimated from the p_T distribution of tracks associated to non-scattered hadrons and leptons, selected in dedicated control samples, by smearing them to take into account the poor p_T resolution of pixel tracklets. The p_T spectrum shape of the fake component is also obtained in a dedicated control region.

The smearing function is extracted from $Z \rightarrow \mu\mu$ events in data by re-fitting the muon candidate track using only the hits in the pixel detector. The $Z \rightarrow \mu\mu$ events are selected by single muon triggers and by requiring two opposite sign muons with difference in azimuthal angle larger than 1.5, and with an invariant mass between 81 GeV and 101 GeV. The q/p_T resolution of pixel tracklets is calculated from the distribution of the difference between the q/p_T of the pixel tracklet and the original standard track. This distribution is shown in Figure 5 (a). The q/p_T difference distribution is modelled by the following

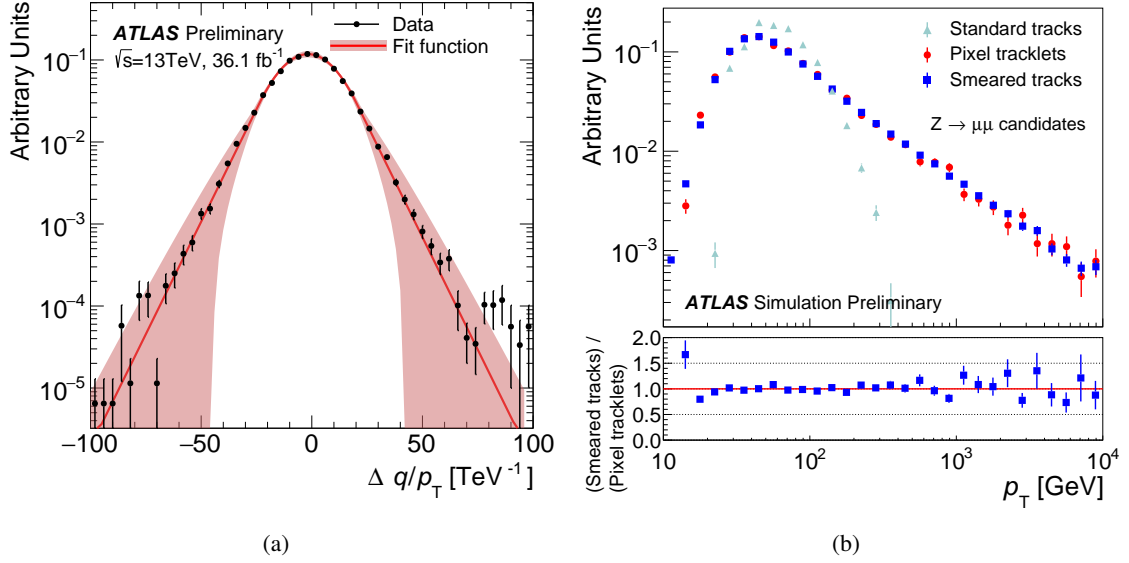


Figure 5: (a) Distribution of the difference of q/p_T of a pixel tracklet and a standard track in $Z \rightarrow \mu\mu$ events in data. The solid line shows the smearing function used to construct the background p_T template, which is described in Section 6.1. The red band indicates a 1σ variation of the systematic uncertainty (see Section 7). The data are normalized to unit area. (b) Validation of the smearing procedure in $Z \rightarrow \mu\mu$ events in simulation. In the upper part, green and red points show the p_T distribution of standard tracks and pixel tracklets, respectively. Blue points show the p_T spectrum obtained by convolving the standard track p_T distribution with the smearing function. In the lower part, the ratio of the distribution of the pixel tracklet and the smeared spectrum is shown.

empirical formula:

$$f(z) = \begin{cases} \exp(\alpha(z + \alpha/2)) & (z < -\alpha) \\ \exp(-z^2/2) & (-\alpha < z < \alpha) \\ \exp(-\alpha(z - \alpha/2)) & (z > \alpha), \end{cases} \quad (1)$$

$$z = \frac{\Delta q/p_T - m}{\sigma}, \quad (2)$$

where m , σ and α are parameters representing the mean, the resolution of the core part of the distribution, and the slope of the tail part, respectively. The measured resolution, for p_T much larger than 10 GeV, is rather poor due to the limited lever-arm of the pixel tracklet. The smearing procedure is validated in simulated $Z \rightarrow \mu\mu$ events, as shown in Figure 5 (b). The p_T spectrum from the refitted pixel tracklets is compared to the one created by convolving the standard track p_T spectrum and the smearing function. The two spectra agree very well up to 12.5 TeV.

Hadron background: Assuming that the p_T spectrum of hadrons scattered in the ID is the same as that of non-scattered hadrons, the p_T spectrum of non-scattered hadrons can be extracted from standard tracks in a control sample of non-scattered hadrons. This assumption has been verified with simulation. The control sample is obtained by applying the same kinematic requirements as for the signal region and then selecting a sample of tracks which satisfy the following requirements:

- The number of associated hits in the TRT must be larger than 15, and associated hits in the SCT must be larger than 6.
- There must be associated energy deposits in the calorimeter: the transverse energy deposited in the calorimeter in a cone of $\Delta R = 0.2$ around the track, excluding the energy cluster associated to the track, (E_T^{cone20}) must satisfy $E_T^{\text{cone20}} > 3$ GeV, and the sum of cluster energies in a cone of $\Delta R = 0.4$ around the track ($\sum_{\Delta R < 0.4} E_T^{\text{clus}}$) and the p_T of the track (p_T^{track}) must satisfy $\sum_{\Delta R < 0.4} E_T^{\text{clus}} / p_T^{\text{track}} > 0.5$.

The p_T spectrum of the control sample is convolved with the smearing function to take into account the resolution of the pixel tracklets. Separate p_T spectra are prepared for the high- E_T^{miss} region and the low- E_T^{miss} region, with the same requirements as the signal region.

Charged-lepton background: In order to obtain the p_T spectrum of background tracklets originating from leptons, events containing exactly one lepton which satisfy the same kinematic requirements as the signal, excluding the lepton-veto, are used. The lepton is required to have an associated inner detector track with $p_T > 16$ GeV which satisfies the tracklet selection, except for the SCT veto and the isolation from leptonic objects.

The p_T distribution of background tracklets from leptons is obtained by multiplying the p_T distribution of the lepton control sample by a transfer factor, which rescales the number of identified leptons to that of pixel tracklets. The transfer factor is p_T dependent for electrons, and η - and ϕ - dependent for muons, as described below.

The transfer factor is extracted with a tag-and-probe method using $Z \rightarrow \ell\ell$ events in data which are selected by a single-lepton trigger. Additional requirements on track-based isolation and 'Tight' likelihood-based identification criteria (in the case of electron) are applied to the lepton used as the tag. The probe lepton is identified by specific track and calorimeter (in the case of electrons) selection criteria discussed below. The tag-probe pair is further required to have an invariant mass within 10 GeV of the Z boson pole mass.

A tag electron is required to fully satisfy electron identification criteria, to match the electron which triggered the event and to have $p_T > 30$ GeV. Probe electrons are identified as clusters of energy in the calorimeter with an associated track satisfying the same quality, isolation, high p_T and geometrical acceptance requirements described in Section 5.1. The probe track has to satisfy either the full pixel tracklet selection or the full electron selection. The transfer factor is defined as the ratio of number of probe electrons which satisfy the full tracklet selection to the number of probe electrons which satisfy the full electron selection, as a function of electron p_T . The transfer factor is $O(10^{-2})$ – $O(10^{-4})$, depending on electron p_T , and is below 10^{-5} for electrons with $p_T > 50$ GeV.

The transfer factor for muons consists of two components: the probability for a muon ID track to be classified as disappearing and the probability for a muon ID track not to have an associated MS track. The first component of the muon transfer factor is estimated with a method similar to that used for the electron transfer factor. The same selection criteria are applied to the tag and probe muons, replacing the electron identification criteria with those for the muon. The first component of the muon transfer factor is found to be 4.5×10^{-4} . The second component is necessary because a MS track is used as a probe to measure the first component, but a MS track veto is applied in the signal region. The second component is evaluated with a similar tag and probe method, where tracks with more than 15 TRT hits are used as a probe, and the probability for an MS track to be matched is calculated. The transfer factor is measured as a function of η and ϕ to fully take into account the detector geometry. The resulting transfer factor for muons is found

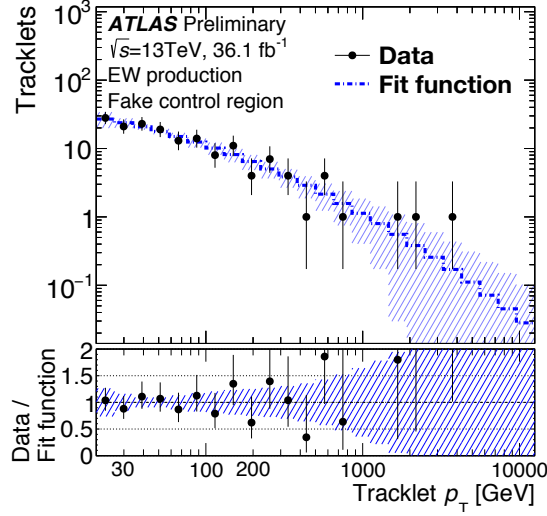


Figure 6: Fit on the fake control sample for the electroweak channel search. The markers show data. The blue line and the band show the fit function and its uncertainty. The bottom plot shows the ratio of the observed data to fit function.

to be of the order of $O(10^{-2})$ to $O(10^{-1})$. The p_T spectra of the lepton control samples are scaled by the transfer factors, then convolved with the smearing function. Two different p_T spectra are prepared, one for the high- E_T^{miss} and one for the low- E_T^{miss} region, while keeping the same requirements as in the signal region.

Fake tracklets: Fake tracklets are tracklets which are seeded from a random combination of hits. The d_0 distribution of fake tracklets is broad, whereas the high- p_T chargino tracklets have good pointing resolution and therefore have values of d_0 which cluster around zero. The fake tracklets control region is defined by requiring $|d_0|/\sigma(d_0) > 10$, and by removing the E_T^{miss} requirement. This region is dominated by fake tracklets. The p_T spectrum of fake tracklets is modelled with the following empirical functional form:

$$f(p_T) = \exp\left(-p_0 \cdot \log(p_T) - p_1 \cdot (\log(p_T))^2\right), \quad (3)$$

where p_0 and p_1 are fit parameters. Figure 6 shows the p_T distribution of pixel tracklets in the fake control region with the result of the fit. The p_T spectrum shape is confirmed to be independent of E_T^{miss} by comparing it in three E_T^{miss} regions: $E_T^{\text{miss}} < 90$ GeV, $90 \text{ GeV} \leq E_T^{\text{miss}} < 140$ GeV and $E_T^{\text{miss}} \geq 140$ GeV. A small dependence of the fit parameters on $|d_0|/\sigma(d_0)$ is observed by comparing the parameters obtained in three regions: $10 \leq |d_0|/\sigma(d_0) < 20$, $20 \leq |d_0|/\sigma(d_0) < 30$ and $30 \leq |d_0|/\sigma(d_0) < 100$. The size of the dependence on $|d_0|/\sigma(d_0)$ is added as uncertainty on the p_T template shape.

Chargino: The signal p_T spectrum is estimated by smearing the truth-particle p_T distribution of charginos in the signal simulation for each signal parameter point. This procedure is performed to reduce the uncertainty of the p_T resolution by computing the parameters of the smearing function mainly based on data. For the signal template, the smearing function parameters measured for muons in data are shifted by the differences in the parameters for charginos and muons observed in the simulation.

6.2 Signal and background fit

The extended likelihood function, described in detail in Appendix A, consists of signal and background components. The background components represent tracklets from muons, fakes, and the sum of hadron and electron contributions. The fit parameters are the signal strength, the normalization of the sum of the hadron and electron, muon, and fake tracklet backgrounds, the fake p_T distribution fit parameters, and nuisance parameters. The nuisance parameters are floating in the fit with Gaussian constraints to include systematic uncertainties, discussed in Section 7. The number of signal and the sum of hadron and electron events are free parameters. The number of muon tracklets and the sum of hadron and electron components are fitted in the low- E_T^{miss} region and in the high- E_T^{miss} region independently. The number of muon events are constrained by the expectation described above. The statistical uncertainty on the transfer factors for muons is propagated to the final template.

The control samples for hadron and electron components are found to have similar p_T distributions, with the same cutoff due to the isolation requirements, and are therefore considered together. The jet-isolation requirement is applied to a tracklet originating from an electron because when a standard track cannot be reconstructed for the electron, a corresponding energy cluster in the calorimeter is identified as a jet. For the sum of hadron and electron component, a single smearing function is used to construct the p_T template.

The fake tracklet control region is divided into two parts, a low- E_T^{miss} and a high- E_T^{miss} fake-tracklet control region, by applying the same E_T^{miss} requirement as in the signal region. The number of fake tracklets in the high- E_T^{miss} region is estimated by multiplying the number of fake tracklets in the low- E_T^{miss} region by the ratio of tracklets in the high- E_T^{miss} fake-tracklet control region and in the low- E_T^{miss} fake-tracklet control region.

7 Systematic uncertainties

An uncertainty on the shape of the hadron and electron p_T template was estimated as the maximum difference between the hadron and electron individual templates and found to be negligibly small. As a combined template is used for hadrons and electrons, the difference in tracklet q/p_T resolutions between hadrons and electrons in simulation is added to the systematic uncertainty on the smearing function for the combined template. The red band in Figure 5 shows the uncertainty of the smearing function.

Possible differences between the signal and the fake control region leading to systematic uncertainties on the p_T spectrum shape are taken into account. The uncertainty is estimated from the d_0 significance dependence of the parameters of the fake spectrum function 3 in the fake-tracklet control region. For the signal p_T resolution, a conservative uncertainty, corresponding to 100% of the effect of multiple scattering, is added to the uncertainty on the parameters of the q/p_T smearing function. A conservative uncertainty of 100% is assigned to the ratio of the fake tracklets in the low- E_T^{miss} and high- E_T^{miss} control regions.

A breakdown of the dominant systematic uncertainties on the expected number of signal events passing the signal region selections is shown in Table 1. Theoretical uncertainties on the signal cross-section are evaluated by computing the changes in the cross-section when the renormalisation and factorisation scales, the choice of PDFs and the strong coupling constant, α_s , are varied. Renormalisation and factorisation scales are varied by factors of 0.5 and 2 times their nominal value. The PDF uncertainty is evaluated as

Relative uncertainties (%)	Electroweak channel	Strong channel
Statistics in simulation	6.6	6.5
ISR/FSR	7.6	0.2
Jet energy scale and resolution	2.0	0.7
Trigger efficiency	0.2	0.0
Pile-up modelling	11.0	4.5
Tracklet efficiency	6.9	
Luminosity	3.2	
Sub-total	16.6	11.3
Cross-section	6.4	28.1
Total	17.8	30.2

Table 1: Systematic uncertainties on the signal event yields at $m_{\tilde{\chi}_1^\pm} = 400$ GeV for the electroweak channel and at $m_{\tilde{g}} = 1800$ GeV, $m_{\tilde{\chi}_1^\pm} = 500$ GeV for the strong channel. The lifetime of chargino is not relevant here.

the maximum of the uncertainty from the CTEQ6.6 [53] uncertainty band at 68% confidence level and the difference between CTEQ6.6 and MSTW2008 NLO [33] PDF sets.

High- p_T jets originating from ISR and final state radiation (FSR) alter the signal acceptance. Uncertainties on the modelling of ISR and FSR are estimated by varying the renormalisation, factorisation and matching scale from 0.5 to 2 times their nominal value, and by comparing samples with one and two additional partons in the matrix element with MG5_aMC@NLO+PYTHIA8. For the strong channel, the ISR/FSR uncertainty is small when the mass difference between the gluino and chargino is large; however, the uncertainty grows to about 10% when the mass difference is smaller than 200 GeV, as signal events start to be rejected by the requirement on the jet p_T . The uncertainties on the jet energy scale and resolution are estimated by the techniques in Refs [42, 54–57]. The pile-up modelling uncertainty is estimated by varying the number of collisions per bunch crossing in simulation by its uncertainty of 10% of the nominal value.

The uncertainty on the chargino reconstruction efficiency can be split into four components: (1) the uncertainty on the probability for a chargino to produce a set of pixel-detector hits which can satisfy the tracklet quality selection, (2) the uncertainty on the efficiency to reconstruct a tracklet when a chargino leaves a set of good hits which satisfies the tracklet quality selection, (3) the uncertainty on the track reconstruction efficiency which depends on the pileup, (4) the uncertainty on the d_0 significance selection. The first component is estimated using $Z \rightarrow \mu\mu$ events, which are selected using the same requirements as for the smearing function data sample. The tracklet quality selection is applied to the muon tracks in the sample, and the difference of the selection efficiency between data and simulation is added to the uncertainty. The second component is estimated by comparing the track reconstruction efficiency of muon tracks in $Z \rightarrow \mu\mu$ events between data and simulation, when muon tracks are required to satisfy the tracklet quality selection. The muon candidate tracks are re-fit using only the pixel hits, and the probability of reconstructing a tracklet is compared between data and simulation. The third component is included in the uncertainty of the pile-up modelling described already. The fourth component is estimated by shifting the measured $|d_0|/\sigma(d_0)$ distribution by its uncertainty; the change of the $|d_0|/\sigma(d_0)$ selection efficiency is added to the systematic uncertainty.

The uncertainty on the trigger efficiency is negligible because it is measured from data, as described in Section 4.

High $E_{\text{T}}^{\text{miss}}$ region	Electroweak channel	Strong channel
	$(m_{\tilde{\chi}_1^\pm}, \tau_{\tilde{\chi}_1^\pm}) = (400 \text{ GeV}, 0.2 \text{ ns}) \quad (m_{\tilde{g}}, m_{\tilde{\chi}_1^\pm}, \tau_{\tilde{\chi}_1^\pm}) = (1600 \text{ GeV}, 500 \text{ GeV}, 0.2 \text{ ns})$	
Number of observed events with $p_{\text{T}} > 100 \text{ GeV}$		
Observed	9	2
Number of expected events with $p_{\text{T}} > 100 \text{ GeV}$		
Hadron+electron background	6.1 ± 0.6	2.08 ± 0.35
Muon background	0.1549 ± 0.0022	0.0385 ± 0.0005
Fake background	5.5 ± 3.3	0.0 ± 0.8
Total background	11.8 ± 3.1	2.1 ± 0.9
Expected signal	10.4 ± 1.7	4.1 ± 0.5
CL_b	0.39	0.702
Observed $\sigma_{\text{vis}}^{95\%}$ [fb]	0.22	0.14
Expected $\sigma_{\text{vis}}^{95\%}$ [fb]	$0.24^{+0.10}_{-0.07}$	$0.11^{+0.06}_{-0.04}$

Table 2: Observed events, background predictions, and expected signal yields for two benchmark models: electroweak channel with $(m_{\tilde{\chi}_1^\pm}, \tau_{\tilde{\chi}_1^\pm}) = (400 \text{ GeV}, 0.2 \text{ ns})$ and strong channel with $(m_{\tilde{g}}, m_{\tilde{\chi}_1^\pm}, \tau_{\tilde{\chi}_1^\pm}) = (1600 \text{ GeV}, 500 \text{ GeV}, 0.2 \text{ ns})$ in the high- E_T^{miss} region. Also shown are the CL_b and the upper limit on the visible cross-section ($\sigma_{\text{vis}}^{95\%}$) at 95% CL.

8 Results

The tracklet p_T spectra are shown in Figure 7, along with the results of the fit to the background-only hypothesis. The observed p_T distributions are well described by the background predictions in the low- E_T^{miss} regions and no significant excess is seen at high tracklet p_T in high- E_T^{miss} regions.

Table 2 lists the observed events yields together with expected background and signal yields in the high- E_T^{miss} region. The number of expected and observed events with a tracklet with p_T above 100 GeV is shown in the table for different background and signal processes. No significant excesses, relative to the expected background, are observed. In order to translate the expected and observed event yields into limits on the signal strength, the profile-likelihood ratio [58] is used as a test statistic, fitting the p_T spectrum in the full range. The confidence levels are computed based on the asymptotic formula in Ref. [58] and following the CL_s prescription [59]. The compatibility with the background-only hypothesis (CL_b) and the upper limits on the visible signal cross-section are shown in Table 2. Data are consistent with the background-only hypothesis.

As no significant excess is found, exclusion limits are computed on the signal strength. Figure 8 shows the exclusion limits in the $(m_{\tilde{\chi}_1^\pm}; \tau_{\tilde{\chi}_1^\pm})$ plane for the electroweak channel, where $\tau_{\tilde{\chi}_1^\pm}$ is the lifetime of the chargino. A large region is excluded by this analysis while the 8 TeV result [16] has higher sensitivity for long lifetimes due to the use of longer tracklets. For $\tau_{\tilde{\chi}_1^\pm} \sim 0.2 \text{ ns}$, which corresponds to $\Delta m_{\tilde{\chi}_1} \sim 160 \text{ MeV}$ in the pure wino LSP model, winos with a mass up to 430 GeV are excluded at 95% CL. Figure 9 shows

the exclusion limits in the $m_{\tilde{g}} - m_{\tilde{\chi}_1^\pm}$ plane for the strong channel. For a chargino lifetime of 0.2 ns, gluino masses up to 1.6 TeV are excluded assuming a chargino mass of 430 GeV, and chargino masses up to 1.05 TeV are excluded assuming very compressed spectra with a mass difference between the gluino and the chargino of less than 200 GeV. Charginos are assumed to decay into a pion and a neutralino in the considered models. However, the presented results do not depend on this decay mode since the decay products of charginos cannot be detected due to their low momentum.

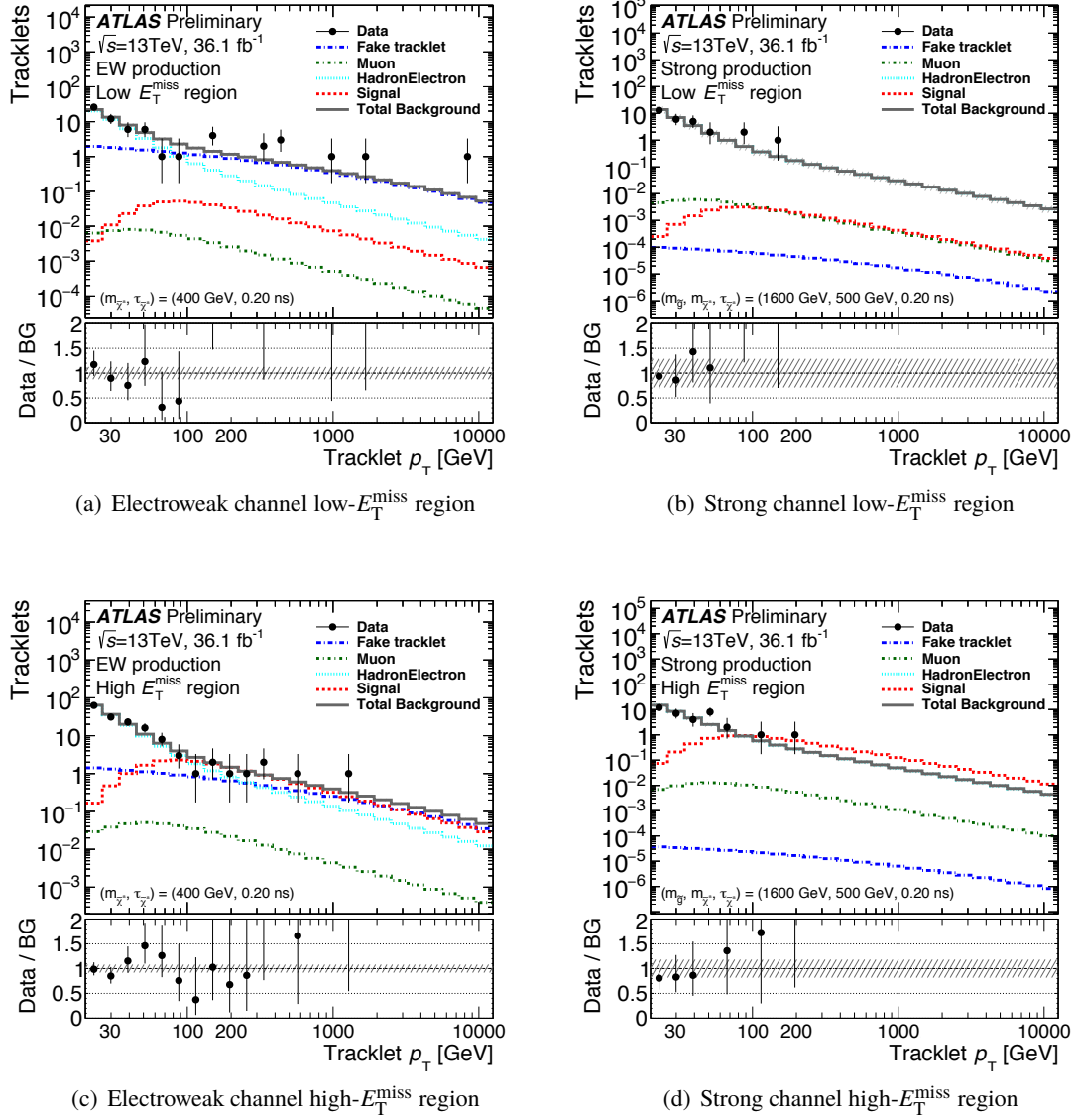


Figure 7: Disappearing tracklet p_T spectrum in various regions. (a) Electroweak channel in the low- E_T^{miss} region. (b) Strong channel in the low- E_T^{miss} region. (c) Electroweak channel in the high- E_T^{miss} region. (d) Strong channel in the high- E_T^{miss} region. Observed data are shown with markers and the background components for the background-only fit are shown with lines. An example of the expected signal spectrum is overlaid for comparison. The bottom panels show the ratio of the data and the background predictions. The error band shows the uncertainty of the background expectation including both statistical and systematic uncertainties.

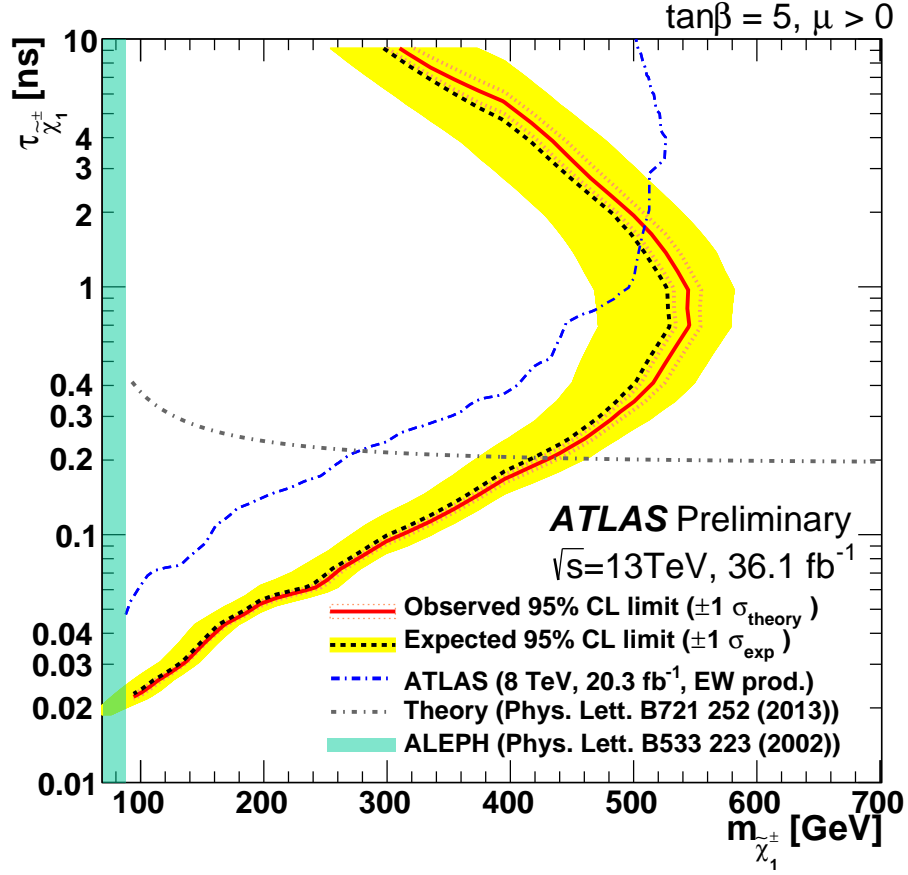


Figure 8: Exclusion limit at 95% CL obtained in the electroweak production channel in terms of the lifetimes and the masses of chargino. The yellow band shows the 1σ region of the distribution of the expected limits. The median of the expectation is shown in a dashed line. The red line shows the observed limit and the orange band around it shows the impact on the observed limit of the variation of the nominal signal cross-section by $\pm 1\sigma$ of its theoretical uncertainties. Results are compared with the observed limits obtained by the previous ATLAS search with disappearing tracklets [16] and an example of the limit obtained at LEP2 by the ALEPH experiment [60]. The lifetime of chargino as a function of the chargino mass are shown in the almost pure wino LSP scenario at the two-loop level [61].

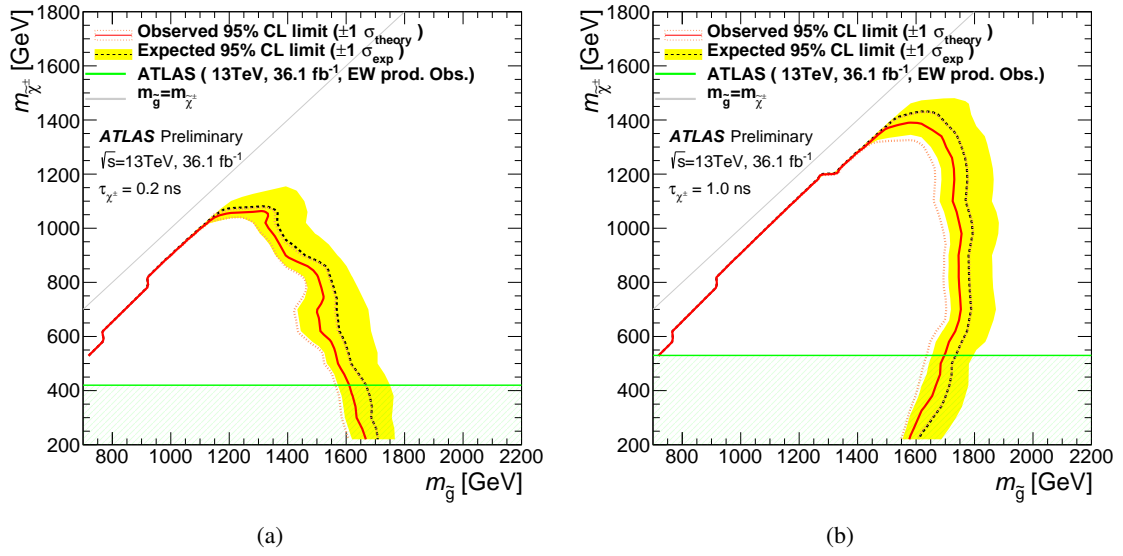


Figure 9: Exclusion limit at 95% CL obtained in the strong production channel in terms of the gluino and chargino masses. The limit is shown assuming a chargino lifetime of (a) 0.2 ns and (b) 1.0 ns. The yellow band shows the 1σ region of the distribution of the expected limits. The median of the expectation is shown in a dashed line. The red line shows the observed limit and the orange band around it shows the impact on the observed limit of the variation of the nominal signal cross-section by $\pm 1\sigma$ of its theoretical uncertainties. Observed limits in the electroweak production search are shown as a green shaded region.

9 Conclusions

A new search for long-lived charginos yielding a pixel tracklet signature was performed based on pp collision data collected by the ATLAS experiment at the LHC in 2015 and 2016 at $\sqrt{s} = 13$ TeV, corresponding to an integrated luminosity of 36.1 fb^{-1} . Tracklets having associated hits only in the pixel detector are used to improve the sensitivity for short chargino lifetimes. The p_T distribution of the pixel tracklets is found to be consistent with the background expectation. A lower limit on $m_{\tilde{\chi}_1^\pm}$ for electroweak production of long-lived charginos for a proper lifetime of 0.2 ns, corresponding to a mass-splitting of 160 MeV, in the pure wino LSP model is set at 430 GeV at 95% CL. In case of charginos produced in the decay cascade of pair-produced gluinos, gluino masses below 1.6 TeV are excluded assuming a chargino mass of 430 GeV, and below 1.05 TeV for compressed spectra with mass difference between the gluino and the chargino of 200 GeV for a proper lifetime of 0.2 ns.

References

- [1] Yu. A. Golfand and E. P. Likhtman, *Extension of the Algebra of Poincare Group Generators and Violation of p Invariance*, JETP Lett. **13** (1971) 323, [Pisma Zh. Eksp. Teor. Fiz.13,452(1971)].
- [2] D. V. Volkov and V. P. Akulov, *Is the Neutrino a Goldstone Particle?*, Phys. Lett. B **46** (1973) 109.
- [3] J. Wess and B. Zumino, *Supergauge Transformations in Four-Dimensions*, Nucl. Phys. B **70** (1974) 39.
- [4] J. Wess and B. Zumino, *Supergauge Invariant Extension of Quantum Electrodynamics*, Nucl. Phys. B **78** (1974) 1.
- [5] S. Ferrara and B. Zumino, *Supergauge Invariant Yang-Mills Theories*, Nucl. Phys. B **79** (1974) 413.
- [6] A. Salam and J. A. Strathdee, *Supersymmetry and Nonabelian Gauges*, Phys. Lett. B **51** (1974) 353.
- [7] G. R. Farrar and P. Fayet, *Phenomenology of the Production, Decay, and Detection of New Hadronic States Associated with Supersymmetry*, Phys. Lett. B **76** (1978) 575.
- [8] G. F. Giudice et al., *Gaugino Mass without Singlets*, JHEP **12** (1998) 027, arXiv: [hep-ph/9810442](#).
- [9] L. Randall and R. Sundrum, *Out of this world supersymmetry breaking*, Nucl. Phys. B **557** (1999) 79, arXiv: [hep-th/9810155](#).
- [10] M. Ibe, S. Matsumoto and R. Sato, *Mass Splitting between Charged and Neutral Winos at Two-Loop Level*, Phys. Lett. B **721** (2013) 252, arXiv: [1212.5989 \[hep-ph\]](#).
- [11] A. J. Barr et al., *Discovering anomaly-mediated supersymmetry at the LHC*, JHEP **03** (2003) 045, arXiv: [hep-ph/0208214 \[hep-ph\]](#).
- [12] ATLAS Collaboration, *Summary of the ATLAS experiment's sensitivity to supersymmetry after LHC Run 1 — interpreted in the phenomenological MSSM*, JHEP **10** (2015) 134, arXiv: [1508.06608 \[hep-ex\]](#).

- [13] C. -H. Chen, M. Drees and J. F. Gunion, *Addendum/erratum for ‘searching for invisible and almost invisible particles at e^+e^- colliders’ [hep-ph/9512230] and ‘a nonstandard string/SUSY scenario and its phenomenological implications’ [hep-ph/9607421]*, (1999), arXiv: [hep-ph/9902309 \[hep-ph\]](#).
- [14] S. Asai et al., *Testing the anomaly mediation at the LHC*, *Phys. Lett. B* **653** (2007) 81 , arXiv: [0705.3086 \[hep-ph\]](#).
- [15] S. Asai, T. Moroi and T. Yanagida, *Test of anomaly mediation at the LHC*, *Phys. Lett. B* **664** (2008) 185 , arXiv: [0802.3725 \[hep-ph\]](#).
- [16] ATLAS Collaboration, *Search for charginos nearly mass degenerate with the lightest neutralino based on a disappearing-track signature in pp collisions at $\sqrt{s} = 8$ TeV with the ATLAS detector*, *Phys. Rev. D* **88** (2013) 112006, arXiv: [1310.3675 \[hep-ex\]](#).
- [17] CMS Collaboration, *Search for disappearing tracks in proton-proton collisions at $\sqrt{s} = 8$ TeV*, *JHEP* **01** (2015) 096, arXiv: [1411.6006 \[hep-ex\]](#).
- [18] ATLAS Collaboration, *The ATLAS Experiment at the CERN Large Hadron Collider*, *JINST* **3** (2008) S08003.
- [19] ATLAS Collaboration, *ATLAS Insertable B-Layer Technical Design Report*, ATLAS-TDR-19 (2010), CERN-LHCC-2010-013, URL: <https://cds.cern.ch/record/1291633>.
- [20] ATLAS Collaboration, *ATLAS Insertable B-Layer Technical Design Report Addendum*, ATLAS-TDR-19-ADD-1 (2012), CERN-LHCC-2012-009, URL: <https://cds.cern.ch/record/1451888>.
- [21] ATLAS Collaboration, *Performance of the ATLAS Trigger System in 2010*, *Eur. Phys. J. C* **72** (2012) 1849, arXiv: [1110.1530 \[hep-ex\]](#).
- [22] ATLAS Collaboration, *2015 start-up trigger menu and initial performance assessment of the ATLAS trigger using Run-2 data*, ATL-DAQ-PUB-2016-001 (2016), ATL-DAQ-PUB-2016-001, URL: <https://cds.cern.ch/record/2136007>.
- [23] ATLAS Collaboration, *Luminosity determination in pp collisions at $\sqrt{s} = 8$ TeV using the ATLAS detector at the LHC*, *Eur. Phys. J. C* **76** (2016) 653, arXiv: [1608.03953 \[hep-ex\]](#).
- [24] F. E. Paige et al., *ISAJET 7.69: A Monte Carlo event generator for pp, $\bar{p}p$, and e^+e^- reactions*, (2003), arXiv: [hep-ph/0312045 \[hep-ph\]](#).
- [25] J. Alwall et al., *The automated computation of tree-level and next-to-leading order differential cross sections, and their matching to parton shower simulations*, *JHEP* **07** (2014) 079, arXiv: [1405.0301 \[hep-ph\]](#).
- [26] T. Sjöstrand et al., *An Introduction to PYTHIA 8.2*, *Comput. Phys. Commun.* **191** (2015) 159, arXiv: [1410.3012 \[hep-ph\]](#).
- [27] NNPDF Collaboration, R. D. Ball et al., *Parton distributions for the LHC Run II*, *JHEP* **04** (2015) 040, arXiv: [1410.8849 \[hep-ph\]](#).
- [28] L. Lönnblad and S. Prestel, *Matching Tree-Level Matrix Elements with Interleaved Showers*, *JHEP* **03** (2012) 019, arXiv: [1109.4829 \[hep-ph\]](#).
- [29] ATLAS Collaboration, *ATLAS Pythia 8 tunes to 7 TeV data*, ATL-PHYS-PUB-2014-021 (2014), URL: <http://cdsweb.cern.ch/record/1966419>.

- [30] W. Beenakker et al., *Squark and gluino production at hadron colliders*, *Nucl. Phys. B* **492** (1997) 51, arXiv: [hep-ph/9610490](#) [hep-ph].
- [31] W. Beenakker et al., *Squark and gluino hadroproduction*, *Int. J. Mod. Phys. A* **26** (2011) 2637, arXiv: [1105.1110](#) [hep-ph].
- [32] P. M. Nadolsky et al., *Implications of CTEQ global analysis for collider observation*, *Phys. Rev. D* **78** (2008) 013004, arXiv: [0802.0007](#) [hep-ph].
- [33] A. D. Martin et al., *Parton distributions for the LHC*, *Eur. Phys. J. C* **63** (2009) 189, arXiv: [0901.0002](#) [hep-ph].
- [34] M. Botje et al., *The PDF4LHC Working Group Interim Recommendations*, (2011), arXiv: [1101.0538](#) [hep-ph].
- [35] ATLAS Collaboration, *The ATLAS Simulation Infrastructure*, *Eur. Phys. J. C* **70** (2010) 823, arXiv: [1005.4568](#) [physics.ins-det].
- [36] S. Agostinelli et al., *GEANT4: A simulation toolkit*, *Nucl. Instrum. Meth. A* **506** (2003) 250.
- [37] ATLAS Collaboration, *Summary of ATLAS Pythia 8 tunes*, ATL-PHYS-PUB-2012-003 (2012), ATL-COM-PHYS-2012-738, URL: <https://cds.cern.ch/record/1474107>.
- [38] ATLAS Collaboration, *Calorimeter Clustering Algorithms: Description and Performance*, (2018), ATL-LARG-PUB-2008-002, URL: <http://cdsweb.cern.ch/record/1099735>.
- [39] M. Cacciari, G. P. Salam and G. Soyez, *The anti- k_t jet clustering algorithm*, *JHEP* **04** (2008) 063, arXiv: [0802.1189](#) [hep-ph].
- [40] M. Cacciari and G. P. Salam, *Dispelling the N^3 myth for the k_t jet-finder*, *Phys. Lett. B* **641** (2006) 57, arXiv: [hep-ph/0512210](#) [hep-ph].
- [41] M. Cacciari and G. P. Salam, *Pileup subtraction using jet areas*, *Phys. Lett. B* **659** (2008) 119, arXiv: [0707.1378](#) [hep-ph].
- [42] ATLAS Collaboration, *Jet Calibration and Systematic Uncertainties for Jets Reconstructed in the ATLAS Detector at $\sqrt{s} = 13$ TeV*, ATL-PHYS-PUB-2015-015, 2015, URL: <https://cds.cern.ch/record/2037613>.
- [43] ATLAS Collaboration, *Tagging and suppression of pileup jets with the ATLAS detector*, ATLAS-CONF-2014-018 (2014), ATLAS-CONF-2014-018, URL: <https://cds.cern.ch/record/1700870>.
- [44] ATLAS Collaboration, *Muon reconstruction performance of the ATLAS detector in proton–proton collision data at $\sqrt{s} = 13$ TeV*, *Eur. Phys. J. C* **76** (2016) 292, arXiv: [1603.05598](#) [hep-ex].
- [45] ATLAS Collaboration, *Topological cell clustering in the ATLAS calorimeters and its performance in LHC Run 1*, (2016), arXiv: [1603.02934](#) [hep-ex].
- [46] ATLAS Collaboration, *Electron efficiency measurements with the ATLAS detector using the 2015 LHC proton-proton collision data*, (2016), ATLAS-CONF-2016-024, URL: <https://cds.cern.ch/record/2157687>.
- [47] ATLAS Collaboration, *Performance of b -Jet Identification in the ATLAS Experiment*, *JINST* **11** (2016) P04008, arXiv: [1512.01094](#) [hep-ex].

- [48] ATLAS Collaboration, *Optimisation of the ATLAS b-tagging performance for the 2016 LHC Run*, (2016), ATL-PHYS-PUB-2016-012, URL: <https://cds.cern.ch/record/2160731>.
- [49] ATLAS Collaboration, *Expected performance of missing transverse momentum reconstruction for the ATLAS detector at $\sqrt{s} = 13$ TeV*, (2015), ATL-PHYS-PUB-2015-023, URL: <https://cds.cern.ch/record/2037700>.
- [50] ATLAS Collaboration, *The Expected Performance of the ATLAS Inner Detector*, (2008), ATL-PHYS-PUB-2009-002, URL: <https://cds.cern.ch/record/1118445>.
- [51] ATLAS Collaboration, *Track Reconstruction Performance of the ATLAS Inner Detector at $\sqrt{s} = 13$ TeV*, (2015), ATL-PHYS-PUB-2015-018, URL: <https://cds.cern.ch/record/2037683>.
- [52] ATLAS Collaboration, *Selection of jets produced in 13TeV proton-proton collisions with the ATLAS detector*, (2015), ATLAS-CONF-2015-029, URL: <https://cds.cern.ch/record/2037702>.
- [53] J. Pumplin et al., *New generation of parton distributions with uncertainties from global QCD analysis*, *JHEP* **07** (2002) 012, arXiv: [hep-ph/0201195](https://arxiv.org/abs/hep-ph/0201195).
- [54] ATLAS Collaboration, *Jet energy measurement with the ATLAS detector in proton-proton collisions at $\sqrt{s} = 7$ TeV*, *Eur. Phys. J. C* **73** (2013) 2304, arXiv: [1112.6426 \[hep-ex\]](https://arxiv.org/abs/1112.6426).
- [55] ATLAS Collaboration, *Single hadron response measurement and calorimeter jet energy scale uncertainty with the ATLAS detector at the LHC*, *Eur. Phys. J. C* **73** (2013) 2305, arXiv: [1203.1302 \[hep-ex\]](https://arxiv.org/abs/1203.1302).
- [56] ATLAS Collaboration, *Monte Carlo Calibration and Combination of In-situ Measurements of Jet Energy Scale, Jet Energy Resolution and Jet Mass in ATLAS*, (2015), ATLAS-CONF-2015-037, URL: <https://cds.cern.ch/record/2044941>.
- [57] ATLAS Collaboration, *Jet energy resolution in proton-proton collisions at $\sqrt{s} = 7$ TeV recorded in 2010 with the ATLAS detector*, *Eur. Phys. J. C* **73** (2013) 2306, arXiv: [1210.6210 \[hep-ex\]](https://arxiv.org/abs/1210.6210), URL: <http://dx.doi.org/10.1140/epjc/s10052-013-2306-0>.
- [58] G. Cowan et al., *Asymptotic formulae for likelihood-based tests of new physics*, *Eur. Phys. J. C* **71** (2011) 1554, arXiv: [1007.1727 \[physics.data-an\]](https://arxiv.org/abs/1007.1727).
- [59] A. L. Read, *Presentation of search results: The $CL(s)$ technique*, *J. Phys. G* **28** (2002) 2693.
- [60] ALEPH Collaboration, A. Heister et al., *Search for charginos nearly mass degenerate with the lightest neutralino in e^+e^- collisions at centre-of-mass energies up to 209 GeV*, *Phys. Lett. B* **533** (2002) 223, arXiv: [hep-ex/0203020 \[hep-ex\]](https://arxiv.org/abs/hep-ex/0203020).
- [61] S. M. Masahiro Ibe and T. T. Yanagida, *PureGravity Mediation with $m_{3/2} = 10$ -100 TeV*, *Phys. Rev. D* **85** (2012), arXiv: [1202.2253 \[hep-ph\]](https://arxiv.org/abs/1202.2253).

Appendix

A Likelihood function

The likelihood function is:

$$\mathcal{L}_{\text{Total}} = \mathcal{L}_{\text{shape}} \times \mathcal{L}_{\text{syst}} \times \mathcal{L}_{\text{syst,fake}} \quad (4)$$

$$\begin{aligned} \mathcal{L}_{\text{shape}} &= \frac{e^{-(n_s^H + n_{h+e}^H + n_\mu^H + n_f^H)}}{n_{\text{obs}}^H!} \cdot \frac{e^{-(n_s^L + n_{h+e}^L + n_\mu^L + n_f^L)}}{n_{\text{obs}}^L!} \\ &\quad \times \prod_{n_{\text{obs}}^H} (n_s^H \mathcal{F}_s^H(p_T; \sigma_s^{\text{smearing}}, \alpha_s^{\text{smearing}}) + n_{h+e}^H \mathcal{F}_{h+e}^H(p_T; \sigma_{h+e}^{\text{smearing}}, \alpha_{h+e}^{\text{smearing}}) \\ &\quad + n_\mu^H \mathcal{F}_\mu^H(p_T) + n_f^H \mathcal{F}_f(p_T; p_0, p_1)) \\ &\quad \times \prod_{n_{\text{obs}}^L} (n_s^L \mathcal{F}_s^L(p_T; \sigma_s^{\text{smearing}}, \alpha_s^{\text{smearing}}) + n_{h+e}^L \mathcal{F}_{h+e}^L(p_T; \sigma_{h+e}^{\text{smearing}}, \alpha_{h+e}^{\text{smearing}}) \\ &\quad + n_\mu^L \mathcal{F}_\mu^L(p_T) + n_f^L \mathcal{F}_f(p_T; p_0, p_1)), \end{aligned} \quad (5)$$

$$\begin{aligned} \mathcal{L}_{\text{syst}} &= \mathcal{N}(\alpha_s^H; \Delta\alpha_s^H) \times \mathcal{N}(\alpha_\mu^H; \Delta\alpha_\mu^H) \times \mathcal{N}(\alpha_s^L; \Delta\alpha_s^L) \times \mathcal{N}(\alpha_\mu^L; \Delta\alpha_\mu^L) \\ &\quad \times \mathcal{N}(\sigma_{h+e}^{\text{smearing}}; \Delta\sigma_{h+e}^{\text{smearing}}) \times \mathcal{N}(\alpha_{h+e}^{\text{smearing}}; \Delta\alpha_{h+e}^{\text{smearing}}) \\ &\quad \times \mathcal{N}(\sigma_s^{\text{smearing}}; \Delta\sigma_s^{\text{smearing}}) \times \mathcal{N}(\alpha_s^{\text{smearing}}; \Delta\alpha_s^{\text{smearing}}), \end{aligned} \quad (6)$$

$$\begin{aligned} \mathcal{L}_{\text{syst,fake}} &= \mathcal{N}(r_{\text{ABCD}}; \Delta r_{\text{ABCD}}) \times \mathcal{P}(n_{\text{FakeCR,obs}}^H | n_{\text{FakeCR}}^H) \times \mathcal{P}(n_{\text{FakeCR,obs}}^L | n_{\text{FakeCR}}^L) \\ &\quad \times \mathcal{N}(p_0; \Delta p_0) \times \mathcal{N}(p_1; \Delta p_1), \end{aligned} \quad (7)$$

$$n_s^H = \mu_s \times \alpha_s^H, \quad (8)$$

$$n_s^L = \mu_s \times \alpha_s^L, \quad (9)$$

$$r_{\text{ABCD}} = \log \frac{n_f^H / n_{\text{FakeCR}}^H}{n_f^L / n_{\text{FakeCR}}^L}, \quad (10)$$

The total likelihood $\mathcal{L}_{\text{Total}}$ consists of three terms: a term for the spectrum shape, $\mathcal{L}_{\text{shape}}$, a term to include systematic uncertainties except for those related to fake background, $\mathcal{L}_{\text{syst}}$, and a term for the fake background uncertainties, $\mathcal{L}_{\text{syst,fake}}$. The numbers of observed events are represented by n_{obs}^R and $n_{\text{FakeCR,obs}}^R$ in the signal region and in the fake control region respectively, where R is H or L , representing the high- E_T^{miss} or the low- E_T^{miss} region. The expected numbers of events for each component (signal, the sum of hadron and electron, muon and fake background) are represented by n_s^R , n_{h+e}^R , n_μ^R and n_f^R respectively. The normalization parameters for the signal and the muon components are represented by α_s^R and α_μ^R . The expected number of signal events is scaled from α_s^R using the relative signal strength μ_s . The probability density functions of those components are represented by \mathcal{F}_s^R , \mathcal{F}_{h+e}^R , \mathcal{F}_μ^R and \mathcal{F}_f . The resolution and slope parameters for the smearing functions are $\sigma_s^{\text{smearing}}$ and $\alpha_s^{\text{smearing}}$ ($\sigma_{h+e}^{\text{smearing}}$ and $\alpha_{h+e}^{\text{smearing}}$) for signal (sum of hadron and electron) respectively. For the fake component, the probability density function is common in the low- E_T^{miss} and in the high- E_T^{miss} regions. The parameters of the fake-spectrum shape function is represented by p_0 and p_1 . The fake ratio factor between the low- E_T^{miss} and high- E_T^{miss} region, r_{ABCD} , is derived from n_f^H , n_f^L and the expected number of events in the fake control regions, n_{FakeCR}^H and n_{FakeCR}^L .

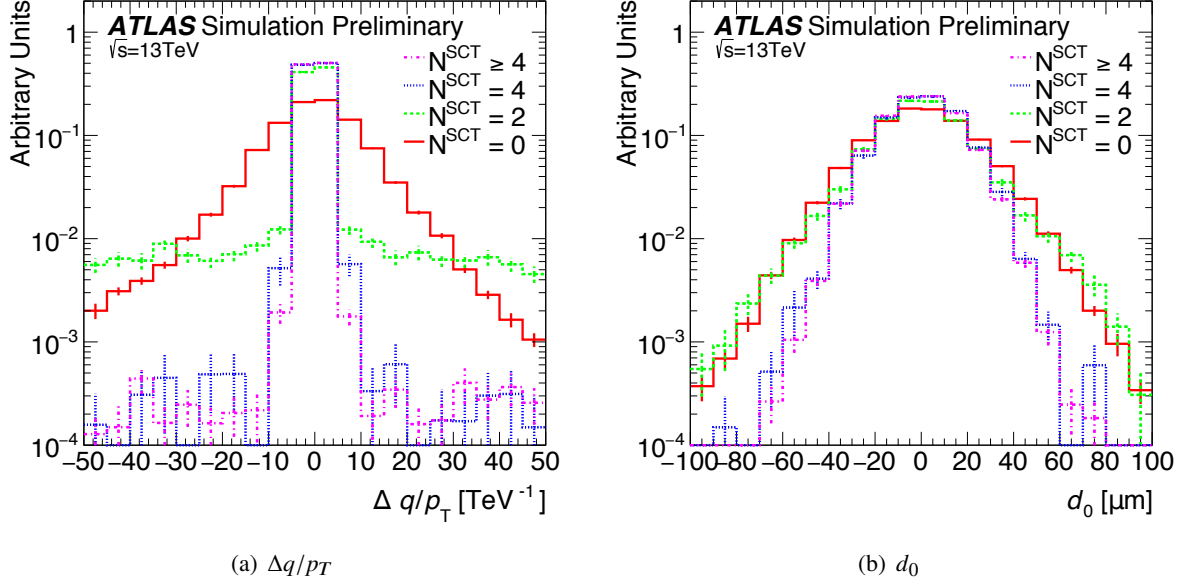


Figure 10: (a) Difference between reconstructed and true q/p_T of tracks (or tracklets for $N^{\text{SCT}} \leq 2$), where N^{SCT} is the number of SCT hits associated to the chargino track (or tracklet). (b) d_0 of tracks (or tracklets). These distributions are extracted from simulated charginos with $p_T > 5$ GeV as a function of N^{SCT} . The truth-level chargino is matched to a reconstructed track (or tracklet) if their azimuthal angular distance is less than 0.05. Each histogram is normalized to unit area.

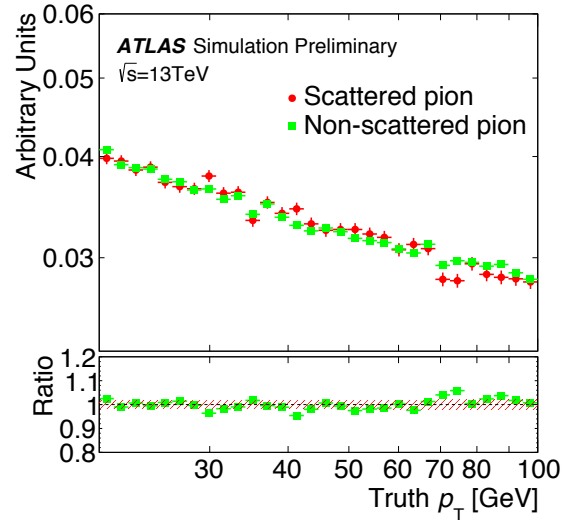
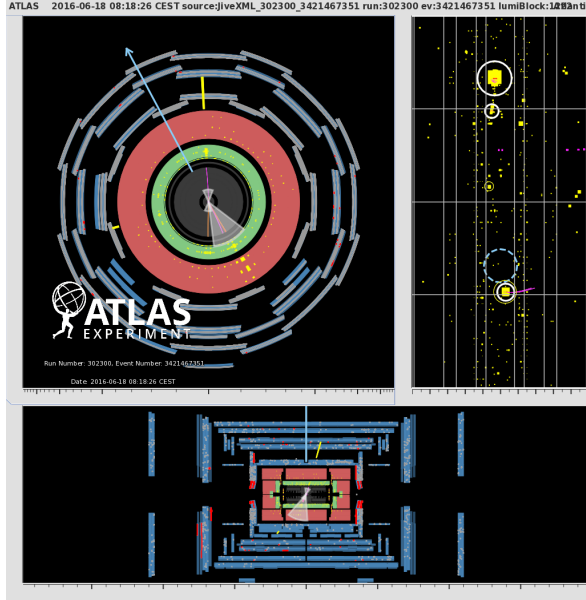
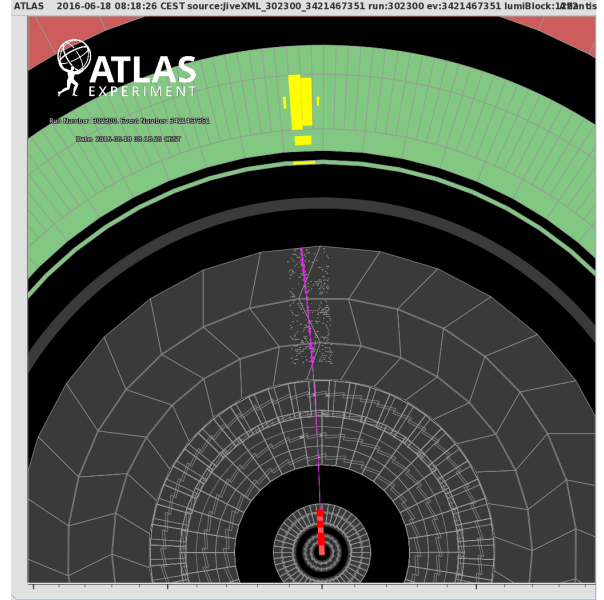


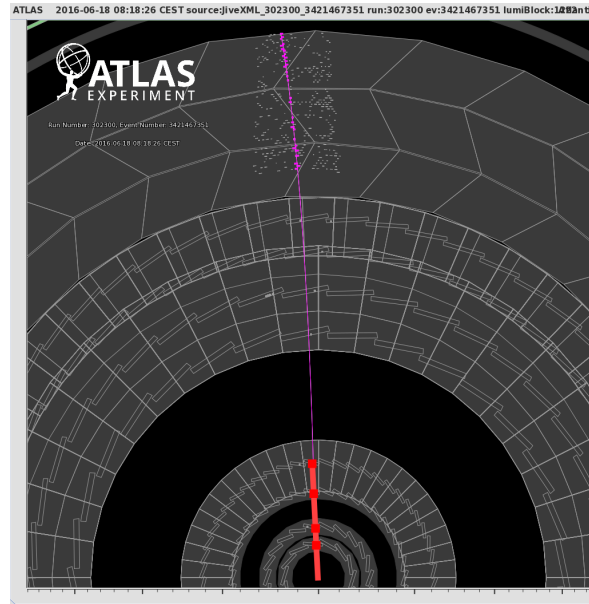
Figure 11: Comparison of truth-level p_T distribution for pions that undergo a hadronic interaction in the ID, and those that do not suffer any hadronic interaction before reaching the calorimeters. Each histogram is normalized to unit area.



(a) Overview



(b) Narrow η and ϕ region.



(c) Enlarged view at ID

Figure 12: Event display of a candidate disappearing track event passing the signal region selection. The red line in the ID represents a disappearing tracklet. The purple line represents a TRT-only track near the disappearing tracklet. White cones represent jets, and the light blue line indicates the missing transverse momentum in the event.